Highly active Pt/In$_2$O$_3$-ZrO$_2$ catalyst for CO$_2$ hydrogenation to methanol with enhanced CO tolerance: The effects of ZrO$_2$

Kaihang Sun [a], Chenyang Shen [a], Rui Zou [a], Chang-jun Liu [a,b,*]

[a] School of Chemical Engineering and Technology, Tianjin University, Tianjin 300350, China
[b] Collaborative Innovation Center of Chemical Science & Engineering, Tianjin University, Tianjin 300072, China

ARTICLE INFO

ABSTRACT

The supported Pt catalyst is normally not active for CO$_2$ hydrogenation to methanol at the presence of CO. Herein, ZrO$_2$ is added into Pt/In$_2$O$_3$ for CO$_2$ hydrogenation to methanol with CO as a co-feed gas. High activity with enhanced CO tolerance is achieved on Pt/In$_2$O$_3$-ZrO$_2$. For example, the space-time yield of methanol reaches 0.569 g$_{methanol}$ g$_{cat}^{-1}$ h^{-1} at 300 °C and 5 MPa under feed gas containing 4% CO of 21,000 cm^3·h^{-1}·g$_{cat}^{-1}$. With the addition of ZrO$_2$, a stronger electron transfer occurs between Pt and the In$_2$O$_3$-ZrO$_2$ solid solution support. This leads to weaker CO adsorption, which suppresses over-reduction of In$_2$O$_3$ and enhances CO tolerance of the Pt catalyst. The oxygen vacancy of In$_2$O$_3$ modified by ZrO$_2$ promotes CO$_2$ activation. The synergy between Zr-modified oxygen vacancy (In-O$_v$-Zr) and Pt catalyst facilitates methanol synthesis from CO$_2$ hydrogenation via formate route. This is different from Pt/In$_2$O$_3$, which takes CO hydrogenation route.

1. Introduction

With the rapid development of renewable energy, CO$_2$ hydrogenation to methanol has attracted increasing attentions worldwide [1]. Cu/ZnO catalyst has been extensively investigated for CO$_2$ hydrogenation to methanol. It is based on the industrial Cu/ZnO catalyst for methanol synthesis from syngas. Studies are being conducted to enhance the activity and improve the stability of Cu/ZnO catalyst [2]. Besides, intensive efforts have been made in recent years to seek for new active catalysts for selective hydrogenation of CO$_2$ to methanol [3–6].

In 2013, our research group predicted, via density functional theory (DFT) studies, that In$_2$O$_3$ with oxygen vacancies is promising for hydrogenation of CO$_2$ to methanol [7]. This prediction was then experimentally confirmed in 2015 [8] and 2016 [9]. The In$_2$O$_3$-based catalysts have now attracted increasing attention because of their high methanol selectivity for CO$_2$ hydrogenation to methanol [10–22]. The oxygen vacancy on In$_2$O$_3$ can promote CO$_2$ activation and hydrogenation, which have been confirmed by experimental [8,9,23] and theoretical studies [7,15,24–26]. To boost the hydrogenation ability of In$_2$O$_3$, various metals, such as Pd [21,22,27], Pt [13,28], Ir [12,29], Au [16], Ag [30], Ru [10], Rh [11,19] and Ni [14,18,31], have been introduced to In$_2$O$_3$. The electronic properties of supported metals can be influenced by the presence of oxygen vacancy on In$_2$O$_3$, resulting in a strong metal-support interaction [25,30]. In addition, the reaction mechanism over the In$_2$O$_3$-based catalysts has been investigated as well. The interface between the metal and defective In$_2$O$_3$ can be considered as the active site for methanol production via the formate, reverse water-gas shift (RWGS) or CO hydrogenation route [25,32,33]. The electronic properties of In$_2$O$_3$ can be tuned by the interplay with ZrO$_2$ as well. Martin et al. [9] and Jiang et al. [34] reported that the surface electronic properties of In$_2$O$_3$ can be modified by the presence of ZrO$_2$, and the stability of intermediates or transition states can be also changed. Yang et al. [35] confirm that the strong electron transfer from ZrO$_2$ to In$_2$O$_3$ plays an important role in methanol synthesis through the formate route. Tsoukalou et al. [36] and Chen et al. [37] made efforts to identify the active phase of In$_2$O$_3$/ZrO$_2$ catalyst for methanol synthesis from CO$_2$ and H$_2$. The In-O$_v$-Zr sites (O$_v$ represents oxygen vacancy), created by the interaction between In$_2$O$_3$ and ZrO$_2$, are crucial for the high activity with the enhanced stability towards methanol production [36]. Frei et al. [38] further demonstrated that the presence of monoclinic ZrO$_2$ favors the formation of more and possibly diverse oxygen vacancies of In$_2$O$_3$. Numpilai et al. [39] found that the higher adsorption of CO$_2$ and H$_2$ on the In$_2$O$_3$/ZrO$_2$ catalyst facilitates methanol production and suppresses the formation of CH$_4$.

On the other hand, the endothermic RWGS reaction to generate carbon monoxide is a side reaction of CO$_2$ hydrogenation to methanol,

---

normally at elevated temperatures. The industrial feed gas of CO_2 hydrogenation usually contains CO as well. The presence of CO would cause the over-reduction of In_2O_3, resulting in deactivation [23]. Furthermore, Araújo et al. [40] reported that the metal-promoted In_2O_3 catalyst (i.e., Pd-In_2O_3 and Ni-In_2O_3) lost nearly 20–40% of the initial activity with the increasing CO concentration in the feed gas. The deactivation can be attributed to the over-reduction of In_2O_3 and the strong adsorption of CO on the supported metals, which inhibits H_2 activation. Therefore, it is necessary to develop the In_2O_3-supported metal catalyst with enhanced CO tolerance. In addition, the supported platinum catalyst has not been confirmed to be active for CO_2 hydrogenation to methanol under the presence of carbon monoxide. It must be helpful from the fundamental aspects if one can make the supported Pt catalyst active for methanol synthesis from a mixture of CO_2 and carbon monoxide.

In this work, we attempted to load ZrO_2 into Pt/In_2O_3 catalyst with a low Pt loading. The obtained Pt/In_2O_3-ZrO_2 catalyst exhibits a high methanol space-time yield (STY) with enhanced CO tolerance at reaction temperature up to 300 °C. From the catalyst characterizations and DFT studies, the addition of ZrO_2 leads to weaker CO adsorption, inhibits the over-reduction induced by CO, promotes the formation of In-O_v-Zr site, and facilitates the methanol production from CO_2 hydrogenation via the formate route.

2. Experimental section

2.1. Catalyst preparation

In_2O_3-ZrO_2 support was prepared via the co-precipitation method. 0.441 g of $ZrO(NO_3)_2 \bullet xH_2O$ (Macklin Biochemical Co., Ltd, Shanghai, 99.5%) and 2.026 g of $In(NO_3)_3 \bullet 4 H_2O$ (HWRK Chem, 99.99%) were dissolved in 50 mL of deionized water, followed by vigorous stirring at 80 °C until fully dissolved. About 3.78 g of $Na_2CO_3 \bullet 10 H_2O$ (Tianjin Kermel Chemical Reagent, 99%) were dissolved in 60 mL of deionized water as the precipitant solution. The precipitant solution was added dropwise into the precursor solution at 80 °C until the pH value reached 9. The mixture was stirred for another 3 h at the same temperature. The precipitate was then washed with deionized water three times. The obtained cake was dried at 80 °C for 12 h prior to calcination in static air at 450 °C for 3 h. The preparation procedure for In_2O_3 was the same as our previous work [28].

The Pt/In_2O_3-ZrO_2 catalyst was synthesized by the deposition-precipitation method. Firstly, a desired amount of platinum nitrate hydrate (Aladdin Chemicals, Shanghai, 18.02 wt% of metal platinum basis) was dissolved in 50 mL of deionized water. Then, 0.4975 g of the as-prepared In_2O_3-ZrO_2 powder was added into the solution, followed by vigorous stirring for 1 h at room temperature. After the temperature reached 80 °C, 0.2 g of urea was added into the mixture under continuous stirring for 3 h. The formed precipitate was washed with 500 mL of deionized water and dried at 60 °C overnight. The as-prepared sample was calcined at 450 °C for 3 h to obtain the Pt/In_2O_3-ZrO_2 catalyst. The Pt/In_2O_3 catalyst was prepared by the same procedure as the Pt/In_2O_3-ZrO_2 catalyst.

2.2. Characterization

The specific surface area (S_{BET}) was calculated using the Brunauer–Emmett–Teller (BET) model based on the 77 K N_2 adsorption/desorption isotherms measured on the ASAP 2460 instrument (Micromeritics).

The chemical components of the catalyst were identified by Inductively Coupled Plasma Optical Emission Spectrometer (ICP-OES) measurements, using a Perkin Elmer Optima 5300DV system.

Powder X-ray diffraction (XRD) was used to investigate the textural structure of the catalyst, using a Rigaku D/max 2500v/pc diffractometer with Cu Kα radiation (40 kV, 200 mA). The scanning rate was set to 4°/

min within the 2θ range of $10°\sim80°$. The phase identification was made by comparison with the Joint Committee on Powder Diffraction Standards (JCPDSs).

Transmission electron microscopy (TEM) measurements were performed on the FEI Titan G2 60–300 microscope equipped with an image corrector. High angle annular dark field scanning TEM (HAADF-STEM) was operated with a Super-X EDX detector system. The sample powder was suspended in ethanol and then dispersed ultrasonically for 5 min. A drop of the suspension was deposited on a copper grid coated with carbon.

X-ray photoelectron spectroscopy (XPS) analyses were performed on a ThermoFischer ESCALAB 250Xi spectrometer using Al Kα ($h\nu$ = 1486.6 eV) radiation. Ar^+ sputtering was used to remove ca. 4 nm of the surface to detect element distribution in the bulk. The spectra of O 1s, In 3d and Zr 3d core level were recorded. The binding energy of C 1s (284.8 eV) was used as a reference for calibration.

Temperature-programmed reduction of hydrogen (H_2-TPR) and temperature-programmed desorption (TPD) of CO and CO_2 experiments, and H_2 pulse experiments were conducted on a Micromeritics Autochem II 2920 chemisorption analyzer equipped with an online HPR-20 EGA mass spectrometer (MS). For the H_2-TPR experiment, about 50 mg of the sample was placed into a U-shaped quartz tube and purged by flowing helium at 200 °C for 1 h. After cooling down to − 10 °C by liquid nitrogen under flowing helium, the sample was then heated to 500 °C at a rate of 10 °C/min under flowing hydrogen (10%). The effluent gas was analyzed by a thermal conductivity detector (TCD). Similarly, for the CO-TPD experiment, about 100 mg of the sample was reduced by the flowing hydrogen (10%) at 200 °C for 1 h. The sample was then purged by flowing helium until the temperature reached 50 °C. After CO adsorption at the same temperature for 1 h, the sample was purged again by flowing helium for 1 h to remove physically absorbed CO. Lastly, the sample was heated to 500 °C at a rate of 10 °C/min. The signals of $m/z =$ 28 and 44 assigned to CO and CO_2 in the effluent gas were recorded by an online mass spectrometer, respectively. The CO_2-TPD experiment was carried out with the same procedure as the CO-TPD experiment except CO_2 was applied as absorbate. As for the H_2 pulse experiments, about 100 mg of the sample was loaded into the U-shaped quartz tube, followed by reduction by a mixture of 10% H_2 in argon at 200 °C for 1 h. After cooling down to 50 °C under flowing helium, 10 pulses of the diluted H_2 (10% hydrogen in argon) were injected into the quartz tube at the same temperature. The metal dispersion was calculated based on the consumption of hydrogen.

An inVia Reflex Renishaw Raman Spectroscopy System with a 532 nm laser as the excitation source was used to obtain the Raman spectra of the samples. The laser power was set at 5 mW and the integration time was 6 s.

The relative amount of oxygen vacancy on the catalyst was analyzed by Electron paramagnetic resonance (EPR) spectra. The measurement was carried out on a Bruker A300 EPR spectrometer operated at the X-band frequency.

2.3. Catalytic activity test

The catalytic activity tests for CO_2 hydrogenation to methanol over the Pt/In_2O_3 and the Pt/In_2O_3-ZrO_2 catalysts were conducted in a vertical fixed bed reactor. 0.2 g of the catalyst, diluted with 1.0 g of SiC, was loaded into the reactor. Prior to the catalytic test, the catalyst was purged by pure N_2 for 0.5 h at room temperature. After reduction under a 10% H_2 flow at 200 °C for 1 h, the feed gas (H_2/CO_2/CO/N_2 = 76/15/4/5 and 76/10/9/5; molar ratio) with a flowrate of 70 Ncm³/min was introduced into the reactor to increase the pressure until the pressure reached 5 MPa. The catalytic activity was measured from 200 to 300 °C with a constant gas hourly space velocity (GHSV) of 21,000 cm³·h⁻¹·g_{cat}⁻¹. The effluent gas was analyzed by an online gas chromatograph (Agilent 7890A) equipped with a two-column system connected to a flame ionized detector (FID) and a thermal conductivity

detector (TCD), respectively. To prevent the condensation of methanol, the valves and lines between the reactor outlet and the GC inlet were heated to 140 °C during the whole test.

CO_2 conversion in methanol synthesis from CO_2-CO hybrids has been simulated and analyzed using the way described in the literature [40]. The methanol STY was calculated based on the molar flowrate of internal insert N_2. The correction factor F is defined as the following equation:

$$F = \frac{A_{methanol}/n_{methanol}}{A_{N_2}/n_{N_2}} \qquad (1)$$

where $A_{methanol}$ and A_{N_2} are the integrated areas of methanol and N_2 in gas chromatography. $n_{methanol}$ and n_{N_2} are the molar flowrate of methanol and N_2. The methanol STY is calculated according to Eq. (2).

$$\text{Methanol STY} = \frac{A_{methanol}}{A_{N_2} \times W_{cat} \times F} \times n_{N_2}^{out} \times M_{methanol} \qquad (2)$$

W_{cat} is the weight of catalyst. $M_{methanol}$ is the molar mass of methanol molecule. $n_{N_2}^{out}$ was calculated based on the N_2 concentration of feed gas and the flowrate.

The CO_2 conversion and methanol selectivity were calculated, based on the composition of the effluent, using the following equations:

$$X_{CO2} = \frac{(F_{CO,out}\text{-}F_{CO,in}) + F_{CH4,out} + F_{methanol,out}}{F_{CO2,out} + (F_{CO,out}\text{-}F_{CO,in}) + F_{CH4,out} + F_{methanol,out}} \times 100\% \qquad (3)$$

$$S_{MeOH} = \frac{F_{methanol,out}}{(F_{CO,out}\text{-}F_{CO,in}) + F_{CH4,out} + F_{methanol,out}} \times 100\% \qquad (4)$$
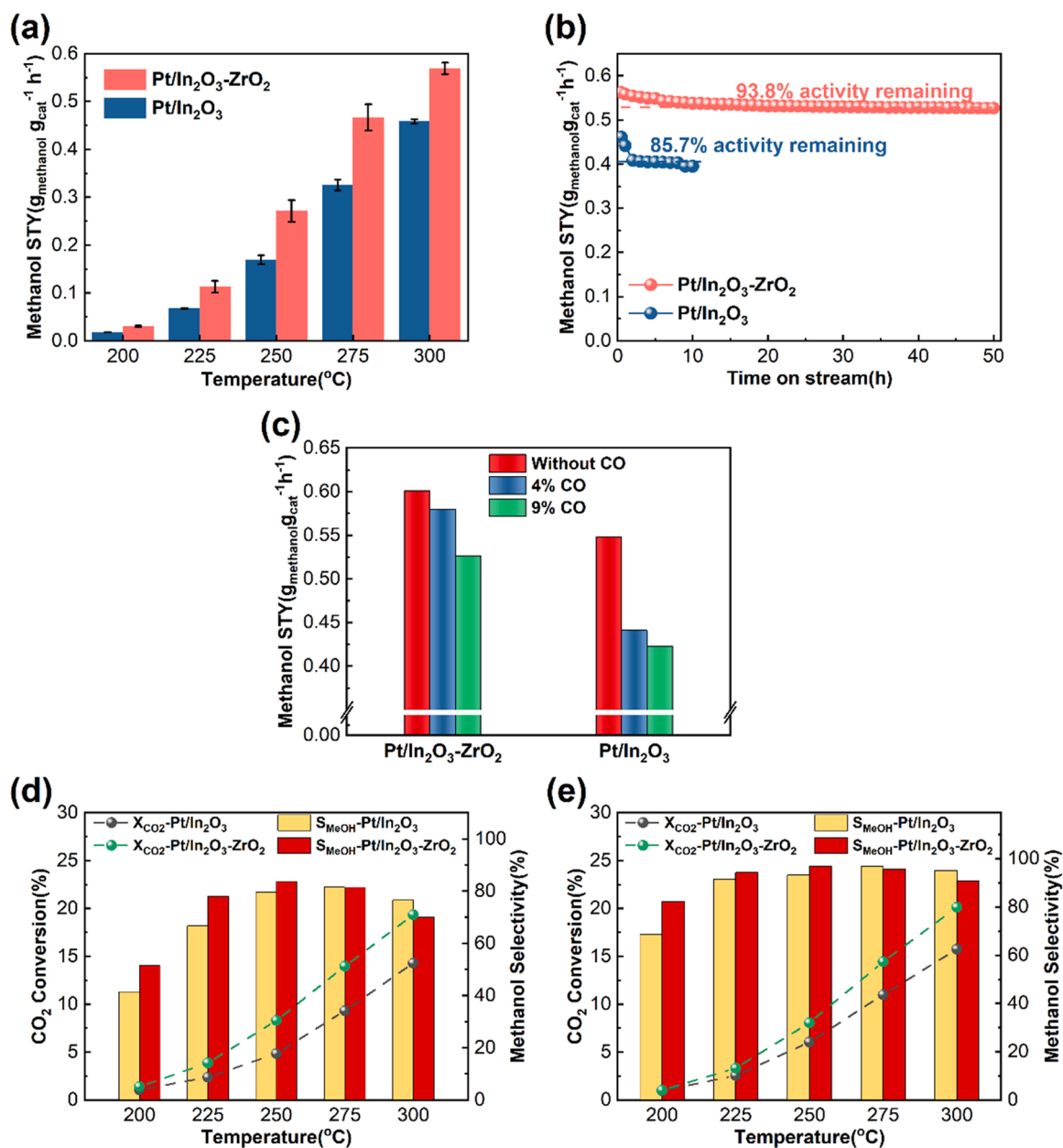
Fig. 1. Catalytic activity tests of the Pt/In$_2$O$_3$-ZrO$_2$ and Pt/In$_2$O$_3$ catalysts. (a) methanol STY from 200 to 300°C under 4% CO in the feed gas; (b) stability at 300 °C for 50 h under 4% CO in the feed gas; (c) methanol STY at 300 °C under different CO concentrations in the feed gas; CO$_2$ conversion and methanol selectivity under (d) 4% and (e) 9% CO in the feed gas. The reaction pressure of all the tests was set to 5 MPa. The carbon balance is 100 ± 1% for all the tests.

$$\text{Carbon balance} = \frac{F_{CO,out} + F_{CO2,out} + F_{CH4,out} + F_{methanol,out}}{F_{CO,in} + F_{CO2,in}} \times 100\% \quad (5)$$

where F represents the molar flowrate of the component in the effluent gas at standard condition. The carbon balance is also examined by Eq. (5).

2.4. DFT calculations

The details of the DFT calculations are given in the Supplementary Information. The defective Pt_4/In_2O_3-ZrO_2(111) surface was constructed in the same way previously used for the study of Pt_4/In_2O_3(111) [25]. The results of ICP-OES, XRD, XPS and Raman spectra indicate that the In_2O_3-ZrO_2 support is in form of solid solution, with which the textural structure is In_2O_3-like but with different electronic structure. Therefore, three In atoms were replaced by Zr atoms in each layer of the In_2O_3(111) slab model with a 12 Å vacuum layer. The dimension of the optimized In_2O_3-ZrO_2(111) slab model was 14.56 Å × 14.56 Å × 20.04 Å. The slab model consisted of 72 O atoms, 9 Zr atoms and 39 In atoms distributed in three In-O-In tri-layers. Similarly, an optimized Pt_4 cluster with a tetrahedral structure was supported on the In_2O_3-ZrO_2(111) surface to obtain the Pt_4/In_2O_3-ZrO_2 model. The oxygen vacancy was created by removing a surface O atom and the defective Pt_4/In_2O_3-ZrO_2 model was named as "Pt_4/In_2O_3-ZrO_2_D". The defective Pt_4/In_2O_3 model was constructed following the same procedures for comparison, which was named as "Pt_4/In_2O_3_D".

3. Results and discussions

3.1. Catalytic activity test

As shown in Fig. 1a, the methanol STY of Pt/In_2O_3-ZrO_2 catalyst reaches 0.569 $g_{methanol} g_{cat}^{-1} h^{-1}$ under the feed gas containing 4% CO with a low Pt loading weight of 0.53 wt% (according to the results of ICP-OES below). It is only 0.458 $g_{methanol} g_{cat}^{-1} h^{-1}$ over the Pt/In_2O_3 catalyst with a similar Pt loading weight of 0.56 wt% under the same condition. The methanol STY based on the loading weight of Pt is also calculated. It is 107.36 $g_{methanol} g_{Pt}^{-1} h^{-1}$ for the Pt/In_2O_3-ZrO_2 catalyst and 80.89 $g_{methanol} g_{Pt}^{-1} h^{-1}$ for the Pt/In_2O_3 catalyst, respectively. This demonstrates that the addition of ZrO_2 to Pt/In_2O_3 cannot only enhance the catalytic activity but also improve the utilization of Pt. Additionally, the results of stability tests, shown in Fig. 1b, indicate that Pt/In_2O_3-ZrO_2 catalyst can maintain 93.8% of the initial activity after a 50-h reaction under 4% CO in the feed gas at 300 °C and 5 MPa, whereas the Pt/In_2O_3 catalyst loses almost 15% of its initial activity after a 10-h reaction. As shown in Fig. 1c, the effect of CO concentration on catalytic activity is investigated as well. The Pt/In_2O_3-ZrO_2 catalyst reaches the highest methanol STY of 0.601 $g_{methanol} g_{cat}^{-1} h^{-1}$ under the feed gas without CO at 300 °C and 5 MPa. This result indicates that the methanol STY on the Pt/In_2O_3 catalyst can be slightly enhanced by the addition of ZrO_2. With the increase of CO concentration in the feed gas, the Pt/In_2O_3-ZrO_2 catalyst remains 96.5% and 88.2% of its activity under 4% and 9% CO concentration at 300 °C and 5 MPa, respectively. However, the Pt/In_2O_3 catalyst loses nearly 19.7% and 24.4% of its activity under the same reaction condition. This further confirms that the enhanced activity with better stability under the CO-containing feed gas is achieved by the addition of ZrO_2. The results of Pt/In_2O_3 catalyst are well consistent with the recent work that the activity of In_2O_3 supported Pd and Ni catalysts is suffered from the presence of CO in feed gas [40]. The CO_2 conversion and methanol selectivity at the presence of carbon monoxide are shown in Fig. 1d and e as well. 19.3% of CO_2 conversion with a high methanol selectivity (>70%) is achieved by the addition of ZrO_2 under the feed gas containing 4% CO at 300 °C and 5 MPa. Due to the increasing H_2/CO_2 ratio in the feed gas containing 9% CO, the CO_2 conversion slightly increases from 14.3% to 15.8% over Pt/In_2O_3 and 19.3 to 20.1% over Pt/In_2O_3-ZrO_2, as shown in Fig. 1e. The

CO_2 conversion over Pt/In_2O_3 is lower than that on Pt/In_2O_3-ZrO_2. This is attributed to the negative effects of over-reduction of In_2O_3 and the poisoning of Pt site by carbon monoxide. The weaker CO adsorption induced by the addition of ZrO_2 facilitates the endothermic RWGS reaction at elevated temperatures, resulting in a lower methanol selectivity over Pt/In_2O_3-ZrO_2 than that over Pt/In_2O_3 at 275 and 300 °C. Table S1 shows a comparison of the reported In_2O_3-based catalysts for the methanol synthesis from CO_2 hydrogenation. Pt is normally formed a bi-metallic catalyst with other metal for CO_2 hydrogenation to methanol, except with In_2O_3 and In_2O_3-ZrO_2 as the support.

3.2. Catalyst characterizations

3.2.1. Textural structure and chemical component

To clarify the chemical components of the as-prepared catalysts, ICP-OES analyses were conducted. As shown in Table 1, the loading weight of Pt of the Pt/In_2O_3-ZrO_2 and Pt/In_2O_3 samples is 0.53 and 0.56 wt%, respectively. The metal dispersion of Pt catalyst of Pt/In_2O_3-ZrO_2 and Pt/In_2O_3 is 78.7% and 43.9%, respectively. The addition of ZrO_2 significantly increases the active Pt sites. The specific surface area of Pt/In_2O_3-ZrO_2 and Pt/In_2O_3 is 112 and 81 m^2/g, respectively. As shown in Fig. 2a-d, the supported Pt nanoparticles are well-dispersed on In_2O_3-ZrO_2 and In_2O_3 with the particle size of ca. 1.26 and ca. 1.88 nm, respectively, after hydrogen reduction at 200 °C for 1 h. The lattice fringe of 0.22 nm can be observed in Fig. 2a and c, which are assigned to Pt(111) facet [28]. The XRD patterns of the Pt/In_2O_3-ZrO_2 and the Pt/In_2O_3 catalysts are shown in Fig. S1. The sample labeled as "H_2 Reduction" in Fig. S1 is the sample after H_2 reduction whereas the sample named as "AR" represents the sample after reaction at 300 °C and 5 MPa. The diffraction peaks of all these ten samples are assigned to In_2O_3 belonging to the $Ia\bar{3}$(206) space group according to PDF#06–0416. The diffraction peaks at 21.5°, 30.7°, 35.5°, 45.7°, 51.0° and 60.7° are assigned to the diffraction from the (211), (222), (400), (431), (440) and (622) planes. No characteristic diffraction peaks of metallic Pt or PtO due to the low Pt loading and the small size of the well-dispersed Pt nanoparticles. As shown in Fig. S2, no additional diffraction peak can be identified over the In_2O_3-ZrO_2 compared with In_2O_3. This indicates that the crystal structure of In_2O_3-ZrO_2 is In_2O_3-like. Su et al. [41] reported that the peak at $2\theta = 21.5°$ distinguishes the bulk phase of In_2O_3 from that of tetragonal ZrO_2. Furthermore, the inset image in Fig. S2 also confirms the downshift of (222) facet of In_2O_3, which is caused by the lattice expansion resulted from penetration of the Zr atom into In_2O_3. The absence of scattering features of Raman spectra for tetragonal ZrO_2 at 642 cm^{-1} indicates that the existence of ZrO_2 is not in the form of tetragonal phase [42]. These results confirm that the In_2O_3-ZrO_2 support is in the form of solid solution. A new diffraction peak located at 33.0° is observed on the Pt/In_2O_3 sample after the reaction at 300 °C and 5 MPa under 9% CO in the feed gas. This peak is assigned to the (101) facet of metallic In, according to PDF#05–0642. This confirms the formation of metallic In after the reaction [40]. As for all the Pt/In_2O_3-ZrO_2 samples, no diffraction peak of metallic In can be observed after the reaction. These results demonstrate that the dramatic decrease of activity on the Pt/In_2O_3 catalyst can be attributed to the over-reduction of In_2O_3 caused by CO in feed gas [23]. The addition of ZrO_2 enhances the stability by suppressing the over-reduction induced
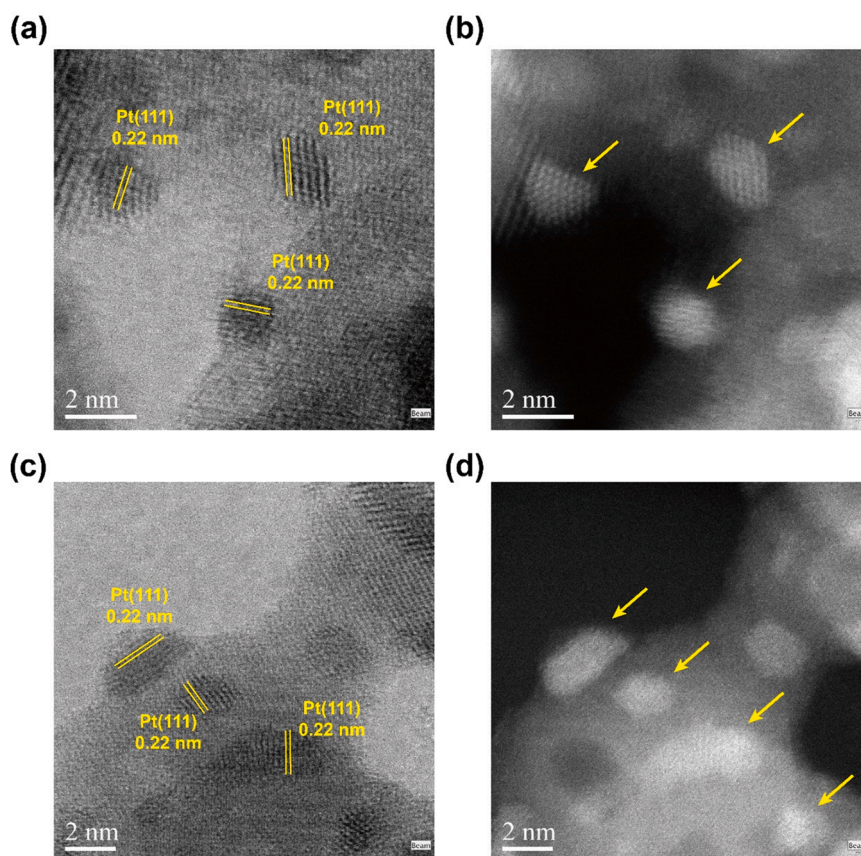
Table 1
The composition, the Pt particle size and dispersion of Pt/In_2O_3-ZrO_2 and Pt/In_2O_3.

Sample	Pt (wt %)	In (wt %)	Zr (wt %)	Pt particle size (nm)	Pt dispersion (%)
Pt/In_2O_3-ZrO_2	0.53	68.46	11.36	1.26[a]	78.7
Pt/In_2O_3	0.56	82.36	/	1.88[a]	43.9

[a] Determined by HAADF-STEM images in Fig. 2.

Fig. 2. (a) TEM image and (b) HAADF-STEM image of Pt/In$_2$O$_3$-ZrO$_2$ sample after H$_2$ reduction, (c) TEM image and (d) HAADF-STEM image of Pt/In$_2$O$_3$ sample after H$_2$ reduction.

by CO under the reaction conditions.

As shown in Fig. 3a, the binding energies located at 444.4 and 452.0 eV are assigned to In 3d$_{5/2}$ and In 3d$_{3/2}$, which confirms the presence of In^{3+} [12]. The In 3d signal exhibits a similar shape and position after Ar$^+$ sputtering, which indicates the stable phase of In$_2$O$_3$ in the catalyst. The binding energies of Zr 3d core level in Fig. 3b centered at 182.2 and 184.6 eV and assigned to Zr 3d$_{5/2}$ and Zr 3d$_{3/2}$, confirm the presence of Zr^{4+} [43]. More importantly, the Zr 3d signals show the unaltered shape and position with a similar intensity as well after Ar$^+$ sputtering. The molar ratio of In/Zr was calculated based on the spectra of the surface and 4 nm ablated by Ar$^+$ sputtering, as shown in Fig. 3d. The molar ratio of In/Zr is 4.8 for the surface and 4.4 for the bulk, close to the result of ICP (4.6) and DFT model (4.3). These indicate the uniform distribution of Zr atoms in both surface and bulk of the catalyst. As shown in Fig. 3c, the binding energies at 529.9 and 531.3 eV can be assigned to the lattice oxygen and the adsorbed oxygen species over oxygen vacancy [36]. The binding energy at 532.3 eV is attributed to the OH group. The relative concentration of oxygen vacancy (C$_{Ov}$) can be calculated by C$_{Ov}$ = A$_{Ov}$/(A$_{Ov}$+A$_{OL}$), where A represents the integrated peak area of the related binding energy in Fig. 3c [27]. The relative concentration of oxygen vacancy for the surface and the bulk of Pt/In$_2$O$_3$-ZrO$_2$ is 25.5% and 15.4%, respectively. This indicates that the presence of Zr in the bulk structure of In$_2$O$_3$ can suppress the over-reduction, resulting in better stability under the reaction conditions. As shown in Fig. S3, the binding energy of In 3d$_{5/2}$ shifts towards a lower value due to the addition of ZrO$_2$. Moreover, the binding energies assigned to lattice oxygen (530.2 to 529.9 eV) and adsorbed oxygen species (531.7 to 531.1 eV) over the oxygen vacancy show an obvious downshift while the binding energy of the Zr 3d core level exhibits the slightly upshift, as shown in Fig. 3b. The electronic structures of In atoms and O atoms on the surface of Pt/In$_2$O$_3$-ZrO$_2$ are regulated by the

addition of ZrO$_2$, which is well distributed in both surface and bulk phases. Combined with the results of XRD, Raman spectra, EPR and XPS, the electronic properties of oxygen vacancy are modified by ZrO$_2$.

3.2.2. Temperature-programmed reduction and desorption experiments

To investigate the H$_2$ activation of the samples, H$_2$-TPR experiments were conducted. As shown in Fig. 4a, the reduction peak centered at 28 °C of the Pt/In$_2$O$_3$-ZrO$_2$ sample and 29 °C of the Pt/In$_2$O$_3$ sample are assigned to the reduction of PtO$_x$ species. The lower intensity of this reduction peak of the Pt/In$_2$O$_3$ sample implies that the Pt species is partially reduced. The H$_2$ consumption peak at 67 °C of the Pt/In$_2$O$_3$ sample can be attributed to the H$_2$ dissociation by Pt species, which shifts towards the lower temperature of 44 °C on the Pt/In$_2$O$_3$-ZrO$_2$ sample. This indicates that the presence of ZrO$_2$ can promote the dissociation and the spillover of atomic H, which is in accordance with the literature [44]. The reduction peaks located at 148 and 194 °C of the Pt/In$_2$O$_3$ sample are assigned to the surface reduction of In$_2$O$_3$ and the reduction of PtO$_x$ species. Due to the lower Pt loading weight, the amount of atomic H generated from Pt species over the present Pt/In$_2$O$_3$ sample is smaller than that over 1.07 wt% Pt/In$_2$O$_3$ sample in our previous work [28]. Therefore, the reduction peak for surface In$_2$O$_3$ can be detected in the H$_2$-TPR profile. No reduction peak of surface In$_2$O$_3$ can be observed on the Pt/In$_2$O$_3$-ZrO$_2$ sample, which is contributed to the more atomic hydrogen and the enhanced stability of surface oxygen atoms resulting from the addition of ZrO$_2$. The mechanism of methanol synthesis can be tuned due to the stabilization of intermediate by ZrO$_2$ [28,45]. In addition, the onset temperature of the bulk reduction of In$_2$O$_3$ is ca. 370 and ca. 440 °C for the Pt/In$_2$O$_3$ and Pt/In$_2$O$_3$-ZrO$_2$ samples, respectively. This is also the evidence that the stability under hydrogen atmosphere can be enhanced by ZrO$_2$.

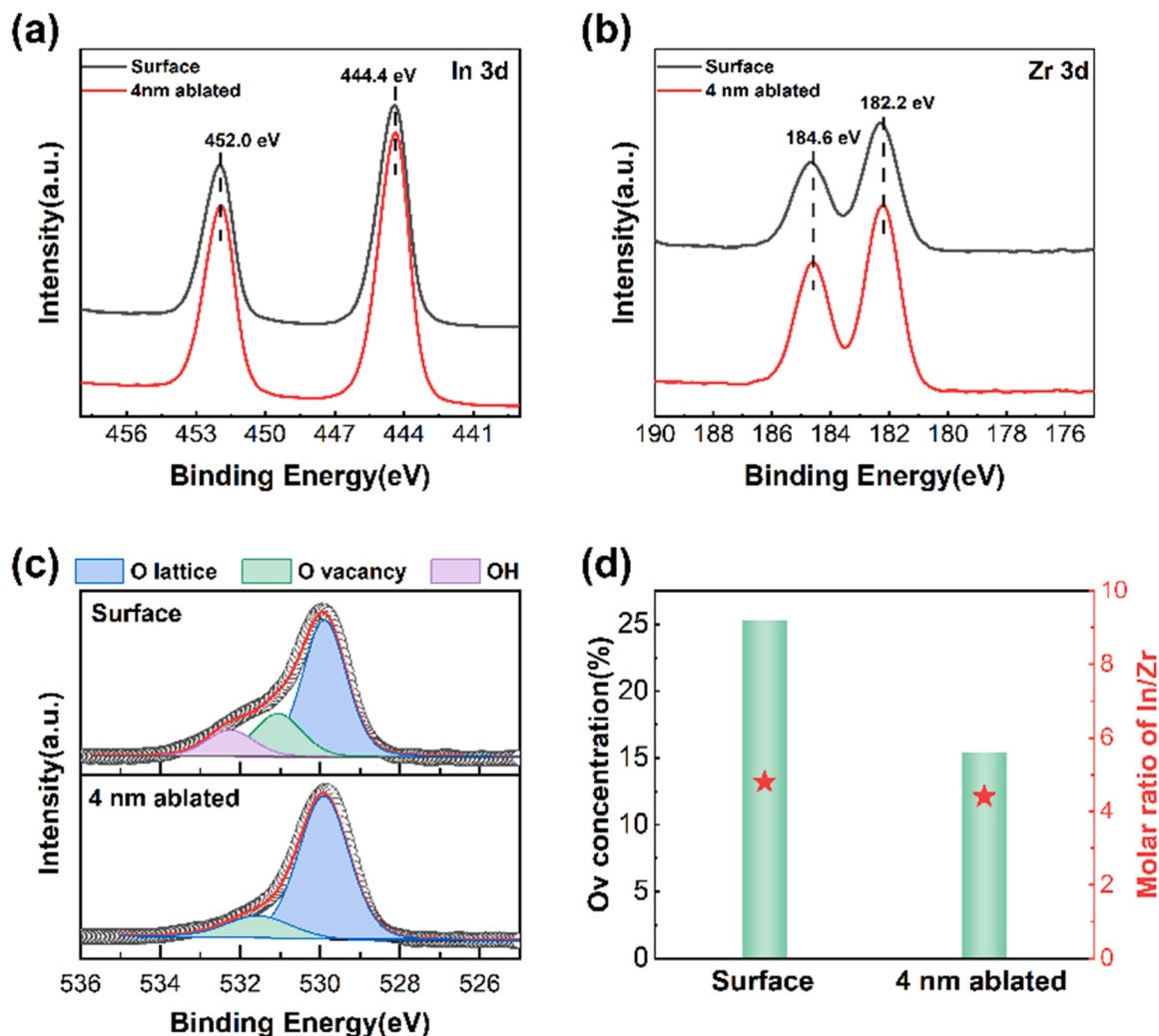As shown in Fig. 4b, the signals of CO evolution are related to the CO

Fig. 3. XPS spectra of Pt/In$_2$O$_3$-ZrO$_2$ with Ar$^+$ sputtering. (a) In 3d (b) Zr 3d and (c) O 1s core level spectra; (d) the relative Ov concentration and the molar ratio of In/Zr based on the spectra of the surface and the bulk via the Ar$^+$ sputtering.
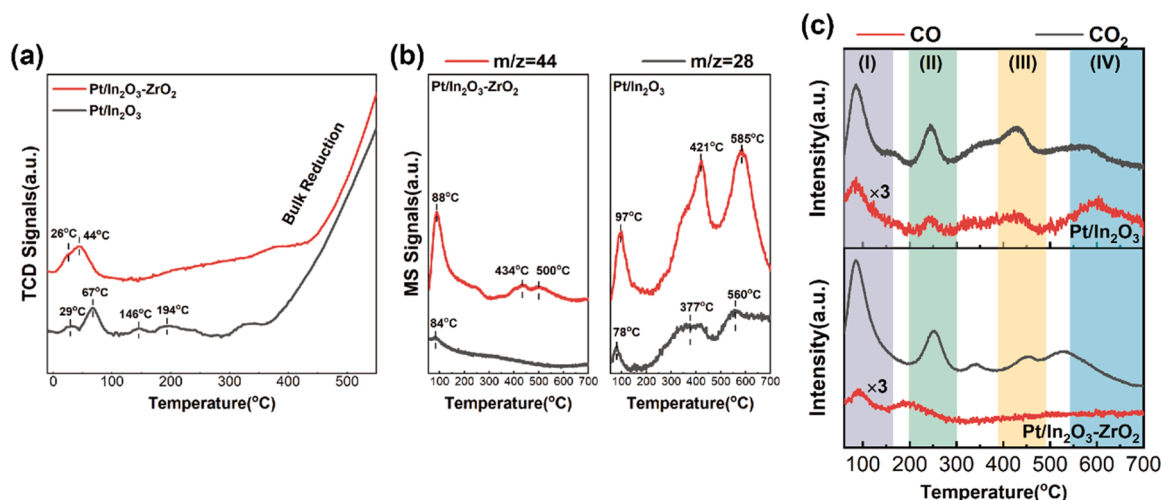

Fig. 4. (a) H$_2$-TPR, (b) CO-TPD-MS and (c) CO$_2$-TPD-MS profiles of the Pt/In$_2$O$_3$-ZrO$_2$ and Pt/In$_2$O$_3$ samples.

desorption from the Pt/In$_2$O$_3$ and Pt/In$_2$O$_3$-ZrO$_2$ samples. The CO desorption peaks lower than 100 °C can be assigned to the physically adsorbed CO on both Pt/In$_2$O$_3$ and Pt/In$_2$O$_3$-ZrO$_2$ samples [30]. No obvious CO desorption peak can be observed on the Pt/In$_2$O$_3$-ZrO$_2$ sample whereas two board CO desorption peaks at 377 and 560 °C are identified to be the moderate and strong CO adsorption sites on the Pt/In$_2$O$_3$ sample. The signals of CO$_2$ evolution are corresponded to the reaction between the sample and the desorbed CO so that the intensity of

the CO_2 desorption peak can be considered as a part of adsorbed CO. The CO_2 desorption peaks at 88 °C for the Pt/In_2O_3-ZrO_2 sample and 97 °C for the Pt/In_2O_3 sample are assigned to the physically adsorbed CO_2 [28]. The CO_2 desorption peaks at 434 and 500 °C on the Pt/In_2O_3-ZrO_2 sample are attributed to the strong CO_2 adsorption sites. The low intensities of these two peaks confirm the weaker CO adsorption over the Pt/In_2O_3-ZrO_2 sample. For the Pt/In_2O_3 sample, two sharp desorption peaks of CO_2 located at 421 and 585 °C on the Pt/In_2O_3 sample can be observed, which confirms the much stronger CO adsorption compared to the Pt/In_2O_3-ZrO_2 sample. These demonstrate that the CO adsorption is significantly inhibited by the addition of ZrO_2. Combined with the results of catalytic tests above, the better stability under the feed gas (containing CO) on the Pt/In_2O_3-ZrO_2 sample benefits from the weaker CO adsorption induced by ZrO_2.

As shown in Fig. 4c, the CO_2 desorption peaks in region (I) are assigned to the physically adsorbed CO_2 while the CO_2 desorption peaks in region (II) can be attributed to the CO_2 desorbed from the oxygen vacancy created by H_2 reduction [9,27]. The peaks in region (III) are contributed to the CO_2 desorbed from the thermal-induced oxygen vacancy [9,27]. The amount of oxygen vacancy induced by H_2 reduction and thermal desorption is decreased by the addition of ZrO_2, which indicates that the stability of surface oxygen atoms of In_2O_3 is improved. The signals of CO evolution confirm the presence of CO_2 dissociation on both Pt/In_2O_3 and Pt/In_2O_3-ZrO_2 samples, which is consistent with the theoretical results of Pt_4/In_2O_3 model catalyst [25]. The lower intensity of CO evolution peak of Pt/In_2O_3-ZrO_2 sample indicates that the CO_2 dissociation is inhibited by the addition of ZrO_2 compared to the Pt/In_2O_3 sample. This suggests that methanol synthesis over Pt/In_2O_3-ZrO_2 catalyst could not take the CO hydrogenation route. The enhanced activity origins from the alternation of reaction mechanism.

3.2.3. Raman and EPR spectra

According to the literature, Raman spectra can be used as an efficient way to quantify the oxygen vacancy over In_2O_3 [46]. Herein, the Raman spectra of the Pt/In_2O_3-ZrO_2 and Pt/In_2O_3 samples are shown in Fig. 5a. The features at ca. 306 (I_1) and ca. 367 (I_2) cm^{-1} are assigned to the bending vibration $\delta(InO_6)$ of octahedra and stretching vibration of In-O-In, respectively [46]. The ratio of I_2/I_1 can characterize the amount of oxygen vacancy on the samples [12,28,30]. The amount of oxygen vacancy on the Pt/In_2O_3-ZrO_2 sample is smaller than that on the Pt/In_2O_3 sample under all conditions. This indicates that the presence of ZrO_2 optimizes the content of oxygen vacancy and improves the stability of surface oxygen atoms. Combined with the results of catalytic tests above, the relationship between the oxygen vacancy and the methanol STY at 300 °C and 5 MPa is shown in Fig. 5b. With the increase of CO concentration in feed gas, the amount of oxygen vacancy on all the samples increases. More importantly, a significant drop of methanol STY with a larger amount of oxygen vacancy can be observed on both two samples. This result confirms the fact that the decrease of methanol STY under the CO-containing feed gas can be attributed to the over-reduction of In_2O_3 resulting from CO. The extra oxygen vacancy formed by the over-reduction induced by H_2 or CO leads to the formation of metallic In and the disordered surface structure [23].

To further characterize the variation of oxygen vacancy as well as the electron transfer property of the catalyst influenced by the addition of ZrO_2, EPR analysis was performed. As shown in Fig. 5c, the intensity of EPR signal can be considered as the relative amount of oxygen vacancy on the sample. The range of magnetic field on each curve is from 3480 to 3545 G. The signal at 3510 G with a g factor of 2.003 on each sample is assigned to the singly ionized oxygen vacancy resulted from the delocalized electrons, which is paramagnetic [9,30]. Also, the intensities of the EPR signals on the Pt/In_2O_3-ZrO_2 sample are lower than that on the Pt/In_2O_3 sample, corresponding to the less oxygen vacancy. This is
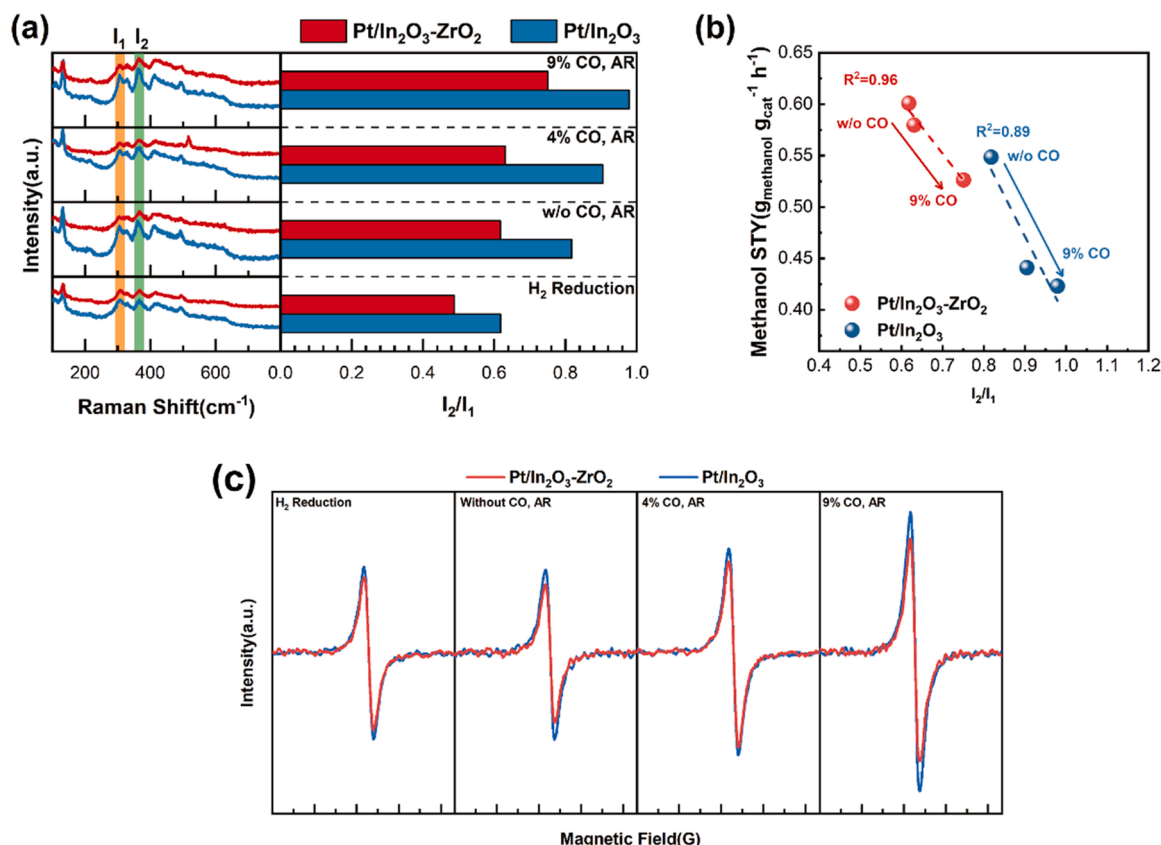

Fig. 5. (a) Raman spectra, (b) the relationship between oxygen vacancy and catalytic activity and (c) EPR spectra of the Pt/In_2O_3-ZrO_2 and Pt/In_2O_3 samples.

consistent with the results of Raman spectra above.

3.3. DFT calculations

3.3.1. The interaction between Pt₄ cluster and the defective In₂O₃-ZrO₂(111)

The optimized structures of the $Pt_4/In_2O_3\_D$ and Pt_4/In_2O_3-ZrO_2_D models are shown in Fig. 6. The average length of Pt-Pt bond on the $Pt_4/In_2O_3\_D$ and Pt_4/In_2O_3-ZrO_2_D models is 2.61 and 2.71 Å, respectively, indicating the stronger interaction between Pt₄ cluster and defective In_2O_3-$ZrO_2(111)$. The adsorption energy of Pt₄ cluster on the defective In_2O_3-$ZrO_2(111)$ is − 8.08 eV, which is much higher than that on the defective $In_2O_3(111)$ (−4.28 eV). This demonstrates that stronger metal-support interaction is created via the addition of ZrO_2. In particular, the In-O_v-In site over the $Pt_4/In_2O_3\_D$ model and the In-O_v-Zr site over the Pt_4/In_2O_3-ZrO_2_D model are highlighted in Fig. 6. As shown in Table 2, the cohesive energy of the Pt₄ cluster on the $Pt_4/In_2O_3\_D$ and Pt_4/In_2O_3-ZrO_2_D models is − 4.09 and − 5.04 eV, respectively. The cohesive energy of the free Pt₄ cluster and Pt bulk is − 3.02 and − 5.26 eV, respectively. These confirm that the stability of Pt₄ cluster is significantly enhanced by the stronger metal-support interaction due to the addition of ZrO_2. The influences of the ZrO_2 on the electronic properties of Pt₄ cluster are investigated as well. As shown in Fig. 7, the d-band center value of the $Pt_4/In_2O_3\_D$ model is − 2.27 eV whereas that of the Pt_4/In_2O_3-ZrO_2_D model shifts away from Fermi level (− 2.43 eV) with the introduction of ZrO_2. This confirms the weaker adsorption of CO molecule [47], which is in accordance with the results of CO-TPD-MS above. Moreover, the total charge of Pt₄ cluster is − 0.16 and − 1.02 | e| for the $Pt_4/In_2O_3\_D$ and Pt_4/In_2O_3-ZrO_2_D models, respectively, based on the results of the Bader charge analyses shown in Fig. S4 and Table S2. The stronger electron transfer from the support to the supported Pt₄ cluster also confirms the presence of stronger metal-support interaction, which is consistent with the results of deformation charge density in Fig. 7.
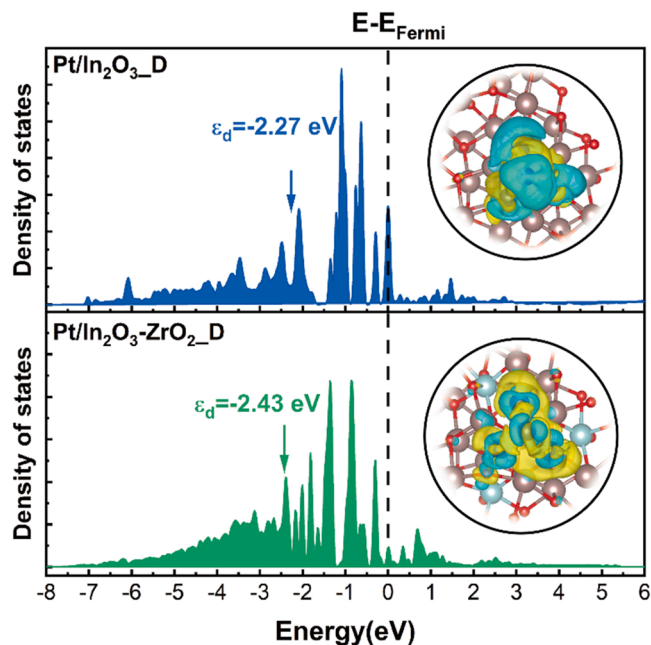
3.3.2. CO adsorption on the Pt_4/In_2O_3-ZrO_2_D model

To investigate the CO adsorption under the reaction conditions, Gibbs free energy of the CO adsorption on the $Pt_4/In_2O_3\_D$ and Pt_4/In_2O_3-ZrO_2_D models is calculated. As shown in Fig. 8a, the Gibbs free energy of CO adsorption on the $Pt_4/In_2O_3\_D$ and Pt_4/In_2O_3-ZrO_2_D models is − 2.28 and − 0.92 eV, respectively, at 200 °C and 5 MPa. The Gibbs free energy of CO adsorption is decreased with the increasing

Table 2
The cohesive energy (CE) of Pt₄ cluster.

	Pt_4/In_2O_3-ZrO_2_D	$Pt_4/In_2O_3\_D$	Pt₄ cluster (free)	Pt bulk
Pt₄ adsorption	-8.08	-4.28		
E_{CE} (eV/per atom)	-5.04	-4.09	-3.02	-5.26

Fig. 7. Projected density of states (PDOS) of Pt 5d orbital and deformation charge density of the $Pt_4/In_2O_3\_D$ and Pt_4/In_2O_3-ZrO_2_D models. Yellow and blue iso-surface represent electron accumulation and depletion, respectively.

temperature due to the promoted CO desorption at the elevated temperature. Under the conditions of 300 °C and 5 MPa, the Gibbs free energy of CO adsorption on the Pt_4/In_2O_3-ZrO_2_D model is − 0.72 eV. The value is much lower than that on the $Pt_4/In_2O_3\_D$ model (−2.11 eV) due to the variation of electronic structure of Pt induced by the introduction of ZrO_2. More importantly, the CO desorption over Pt/In_2O_3 is
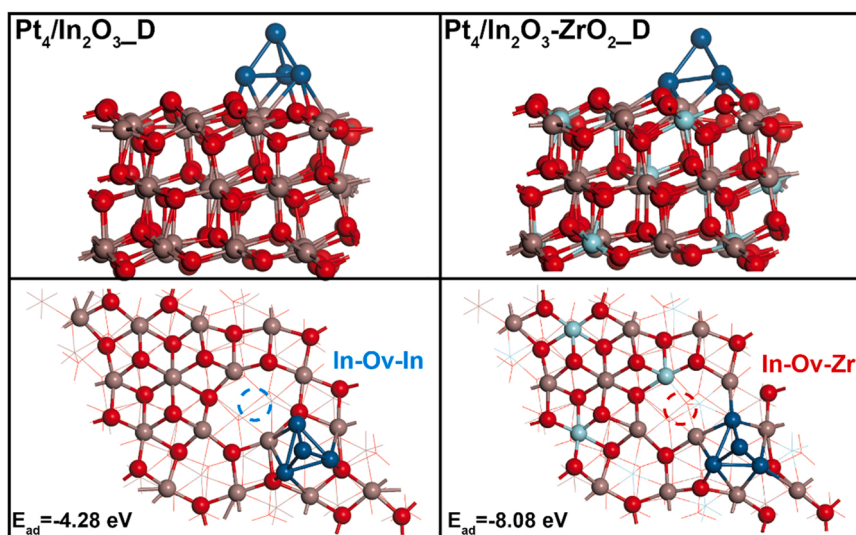
Fig. 6. Optimized structures of the $Pt_4/In_2O_3\_D$ and Pt_4/In_2O_3-ZrO_2_D models. The dash line cycles in blue and red represent In-O_v-In and In-O_v-Zr site, respectively. Blue: Pt atoms; red: O atoms; Brown: In atoms; cyan: Zr atoms.
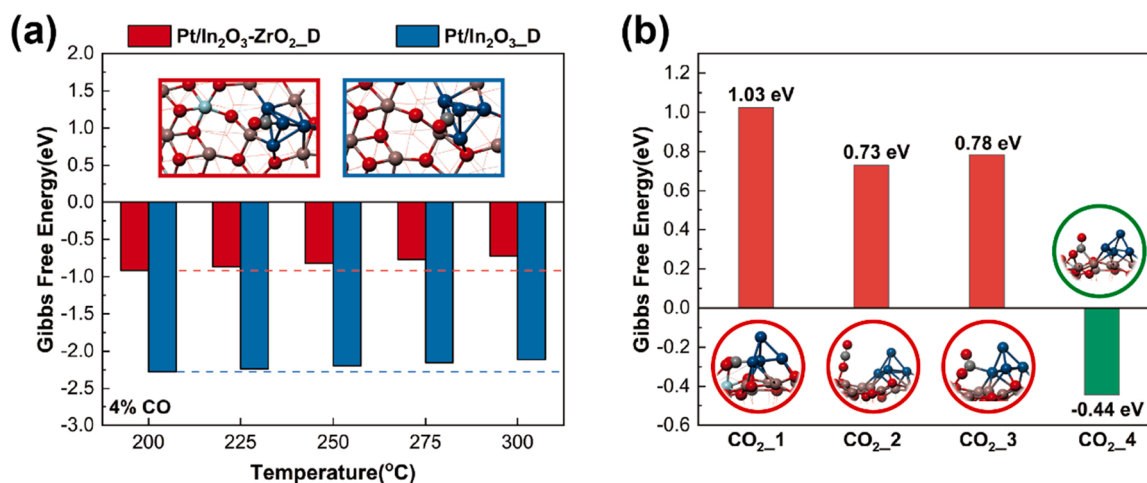
Fig. 8. (a) CO and (b) CO_2 adsorption on the $Pt_4/In_2O_3\_D$ and Pt_4/In_2O_3-ZrO_2_D models under the reaction conditions.

difficult with the presence of CO in the feed gas even at high temperature. In contrast, the CO adsorbed on the Pt site of Pt/In_2O_3-ZrO_2 catalyst prefers to be desorbed to gas phase and releases the active Pt site for H_2 activation, leading to the enhanced activity under the feed gas containing CO.

3.3.3. CO_2 activation on the $Pt_4/In_2O_3\_D$ model

CO_2 activation on the $Pt_4/In_2O_3\_D$ model has been studied in our previous work [25]. The interfacial site between Pt_4 cluster and the surface oxygen vacancy of In_2O_3 is the active site for CO_2 activation. In the present work, four potential active sites for CO_2 activation on the Pt_4/In_2O_3-ZrO_2_D model are investigated under the conditions of 5 MPa and 300 °C as shown in Fig. 8b. CO_2 molecule can be activated at the interface of Pt_4 cluster and defective In_2O_3-ZrO_2 surface to form bi-CO_2 * and mono-CO_2 *, which are marked as CO_2-1 and CO_2-3. The additional Zr site can be considered as the active site for CO_2 activation as well, which is named as CO_2-2. The presence of In-O_v-Zr site is confirmed by Tsoukalou et al. [36] on the In_2O_3/m-ZrO_2 catalyst. CO_2-4 represents the CO_2 molecule activated on the In-O_v-Zr site. The Gibbs adsorption energies of CO_2-1, CO_2-2 and CO_2-3 are positive values, which are 1.03, 0.73 and 0.78 eV, respectively. This indicates that the CO_2 activation on these three sites is not thermodynamically favorable, which leads to CO_2 desorption under the reaction conditions. In contrast, the Gibbs adsorption energy of CO_2-4 is − 0.44 eV, which confirms that the CO_2 activation on this site is the most

thermodynamically favorable among these four sites. Based on the discussions above, CO_2-4 is the most stable configuration of CO_2 activation on the Pt_4/In_2O_3-ZrO_2_D model. This configuration was thus used for the study of the reaction mechanism of methanol synthesis.

3.3.4. The reaction mechanism of CO_2 hydrogenation to methanol over the Pt_4/In_2O_3-ZrO_2_D model

According to the literature, ZrO_2 can promote the dissociation and spillover of H_2 as well as the stabilization of reaction intermediates [44]. The CO hydrogenation route, the RWGS route and the formate route are investigated to clarify the effects of ZrO_2 on the formation and conversion of CO in different routes. The Gibbs free energy profile is shown in Fig. 9. The activation of CO_2 at the In-O_v-Zr site is exergonic by − 0.44 eV through R1, which confirms that the In-O_v-Zr site is favorable for CO_2 activation under the reaction conditions. The CO hydrogenation route, initiated with the dissociation of CO_2 through R3 (Figs. S5 and S6), is studied firstly. This reaction is exergonic by − 2.22 eV with a Gibbs activation barrier of 0.25 eV. This process is both kinetically and thermodynamically favorable. Since the activation barrier of CO_2 dissociation over the defective $Pt_4/In_2O_3\_D$ model (0.18 eV without correction) [25] is lower than that on the Pt_4/In_2O_3-ZrO_2_D model (0.31 eV without correction), the CO_2 dissociation is suppressed by the addition of ZrO_2. Additionally, the backward Gibbs activation barrier for this reaction reaches 2.46 eV, which implies that the stability of surface O atoms is significantly enhanced by the introduction of ZrO_2 so that the
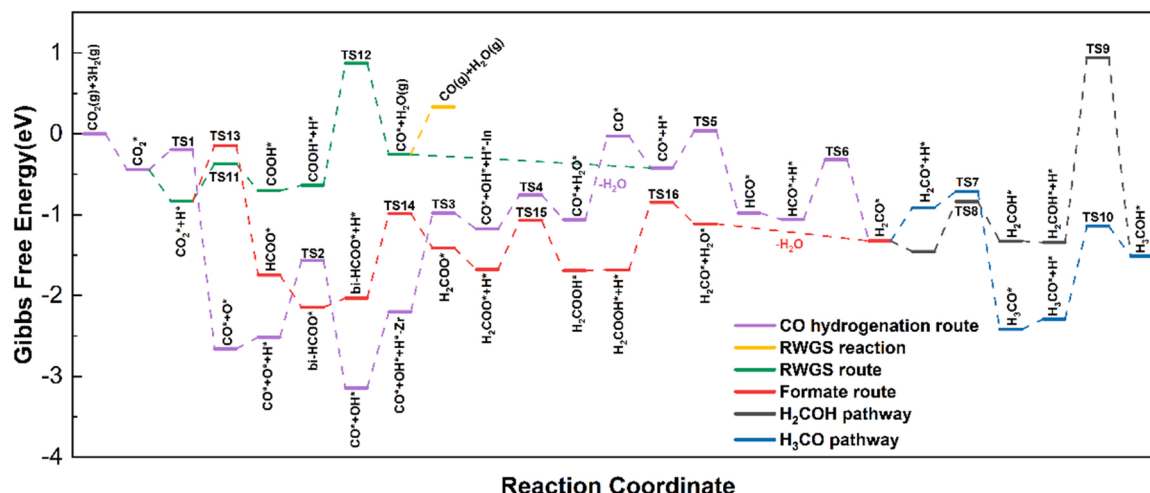

Fig. 9. Gibbs free energy profile of the methanol synthesis on the Pt_4/In_2O_3-ZrO_2 model at 300 °C and 5 MPa.

formation of oxygen vacancy by CO reduction is highly blocked. This is consistent with the results of CO_2-TPD-MS profiles, EPR spectra and Raman spectra above. The surface O* can react with H*, activated by the Pt_4 cluster through R4 to generate the OH*. This reaction is also kinetically and thermodynamically favorable with the Gibbs activation barrier of 0.95 eV and the Gibbs reaction energy of − 0.63 eV. The produced OH* adsorbed on Zr site can migrate to another In site during the H_2 activation on the Pt site through R5, which is endergonic by + 1.03 eV with a Gibbs activation barrier of 1.22 eV. The activated H* can continuously react with OH* to form surface H_2O* through R6, which is endergonic by + 0.12 eV with a Gibbs activation barrier of 0.42 eV. CO* can react with a H* to generate HCO* via R8 after H_2O desorption through R7. This reaction is exergonic by − 0.56 eV with a Gibbs activation barrier of 0.46 eV. However, the H_2 activation of CO* +OH* and the following migration of OH* are endergonic by 0.94 and 1.22 eV, respectively. This indicates that the hydrogenation of CO* +OH* is both kinetically and thermodynamically unfavorable. The presence of CO* on Pt_4 cluster inhibits the H_2 activation significantly. H_2CO* can be generated by the hydrogenation of HCO* through R9, which is exergonic by − 0.26 eV with a Gibbs activation barrier of 0.74 eV. H_3CO* and H_2COH* can be produced by the hydrogenation of H_2CO* through R10 and the protonation of H_2CO* through R11, respectively. The hydrogenation of H_2CO* is strongly exergonic by − 1.51 eV with a Gibbs activation barrier of 0.20 eV whereas the protonation of H_2CO* is endergonic by + 0.13 eV with a Gibbs activation barrier of 0.62 eV. This indicates that the production of H_3CO* is more kinetically and thermodynamically favorable than the production of H_2COH* due to the lower Gibbs activation barrier and the exergonic nature. H_3CO* can react with a H* spillover from the Pt_4 cluster to the support surface to produce H_3COH* through R12. This reaction is endergonic by + 0.78 eV with a Gibbs activation barrier of 1.15 eV. H_3COH* can be produced by the hydrogenation of H_2COH* through R13 as well, which is exergonic by − 0.17 eV with a huge Gibbs activation barrier of 2.29 eV. This demonstrates that the hydrogenation of H_2COH* to H_3COH* is kinetically hindered so that the production of H_3COH* tends to undergo R12 rather than R13.

As for the RWGS route, CO_2 * reacts with H* to form COOH* through R14 initially. This reaction is slightly endergonic by + 0.13 eV with a Gibbs activation barrier of 0.46 eV. The hydrogenation of COOH*- through R15 is endergonic by + 0.38 eV with a high Gibbs activation barrier of 1.51 eV. On one hand, the produced CO* and H_2O* desorbed from the active site with the Gibbs free energy cost of + 0.59 eV. On the other hand, CO* can react with H* through R8 and produce H_3COH* after a series of elementary steps as mentioned above. This confirms that CO* prefers to react with H* rather than to be desorbed due to the lower Gibbs activation barrier of 0.46 eV. CO produced from COOH* is inhibited by the addition of ZrO_2, which is in accordance with the literature [34].

The formate route is blocked due to the high activation barrier of the initial hydrogenation of CO_2 * to HCOO* over the defective Pt_4/In_2O_3 model [25]. Herein, the formate route is also calculated to investigate the effects of ZrO_2 on the reaction mechanism. The formate route is initiated with the direct hydrogenation of CO_2 to HCOO* through R17, which is exergonic by − 0.92 eV with a Gibbs activation barrier of 0.68 eV. This reaction is switched to the kinetically and thermodynamically favorable step via the addition of ZrO_2. The formed mono--HCOO* is not stable and tends to transform to the more stable bi-HCOO* via R18 without any activation barrier [32]. The bi-H-COO* can react with a spillover H* on the catalyst surface to produce H_2COO* via R19, which is endergonic by + 0.62 eV with a Gibbs activation barrier of 1.05 eV. The product of hydrogenation of H_2COO* is H_2COOH*. The formation of H_2COOH* through R20 is slightly exergonic by − 0.02 eV with a Gibbs activation barrier of 0.61 eV. As the important intermediate of methanol synthesis from CO_2 and H_2, H_2CO* is produced by the hydrogenation of H_2COOH* through R21. This process is endergonic by + 0.57 eV with a Gibbs activation barrier

of 0.83 eV. After the desorption of H_2O via R22, the formed H_2CO* can subsequently react with H* to H_3COH* via a series of elementary steps.

3.3.5. The effect of the ZrO_2 addition on the hydrogenation of CO_2

The formate route, RWGS route and CO hydrogenation route for methanol synthesis from CO_2 hydrogenation over the defective Pt/In_2O_3 catalyst have been studied in our previous work [25]. As for the formate route, the activation barrier of HCOO* formation is 1.60 eV, indicating that this route is kinetically unfavorable on the Pt_4/In_2O_3_D model. The RWGS route suffers from the high barrier of further hydrogenation of the produced CO* (by COOH*). Therefore, the formate route and the RWGS route are not feasible for methanol synthesis over the Pt/In_2O_3 catalyst. The activation barrier of CO_2 dissociation is increased from 0.18 to 0.31 eV induced by the ZrO_2-modification. More importantly, the CO hydrogenation route is hindered by the huge Gibbs free energy for H_2 activation and CO* hydrogenation on the Pt_4/In_2O_3-ZrO_2_D model, while these reactions are favorable (CO_2*→CO*→HCO*→H_2CO* →H_3CO*→H_3COH*) on the Pt_4/In_2O_3_D model. The active site for CO_2 conversion is altered from the interfacial site to the In-O_v-Zr site due to the addition of ZrO_2. The formation of HCOO* on the Pt_4/In_2O_3-ZrO_2_D model is kinetically and thermodynamically favorable, which is exergonic by − 0.92 eV with the Gibbs activation barrier of 0.68 eV. In addition, the hydrogenation of COOH* is not feasible due to the huge Gibbs activation barrier of 1.51 eV so that the RWGS route is kinetically blocked. Thus, the results of DFT calculations confirm that the reaction mechanism of methanol synthesis from CO_2 hydrogenation over the $Pt-In_2O_3$ system is altered by the addition of ZrO_2.

3.3.6. The effect of produced H_2O over the Pt_4/In_2O_3-ZrO_2_D model

The effect of H_2O produced via R21 on the methanol synthesis from H_2CO* was investigated (Fig. S7). The hydrogenation of H_2CO* to H_3CO* via R23 is exergonic by − 1.25 eV with a Gibbs activation barrier of 0.59 eV. The protonation of H_2CO* to H_2COH* through R24 is exergonic by − 0.14 eV with a Gibbs activation barrier of 0.40 eV. Compared with the results of R9 and R10, the adsorbed H_2O* facilitates the formation of H_2COH* due to the lower Gibbs activation barrier and the alteration from endergonic to exergonic. However, the formation of H_3CO* is inhibited by the presence of H_2O* due to the higher Gibbs activation barrier. Furthermore, the production of H_3COH* from H_3CO* via R25 is endergonic by + 0.89 eV with a Gibbs activation barrier of 1.34 eV, which is kinetically and thermodynamically unfavorable compared to R11. The hydrogenation of H_2COH* to H_3COH* through R26 is exergonic by − 0.23 eV with a Gibbs activation barrier of 1.79 eV. This reaction is still kinetically hindered due to the high activation barrier. These suggest that the presence of adsorbed H_2O* is unfavorable for methanol production.

All of the elementary steps with the Gibbs free energies and activation barriers are summarized in Table 3. The structures of the initial, transition and final states are shown in Fig. S5 in detail. The structures of adsorbed species involved in methanol production are shown in Fig. S6.

In summary, the In-O_v-Zr site is created by the addition of ZrO_2, which modulates the electronic properties of oxygen vacancy as well as the supported Pt_4 cluster. The presence of ZrO_2 inhibits the CO formation from COOH* and decreases the CO adsorption over the Pt_4/In_2O_3-ZrO_2_D model. The synergy between the In-O_v-Zr site and Pt_4 cluster can facilitate methanol production through the formate route as: CO_2* →HCOO* →H_2COO* →H_2CO* →H_3CO* →H_3COH*.

4. Conclusions

From the experimental and theoretical studies discussed above, the Pt/In_2O_3-ZrO_2 catalyst, prepared via the deposition-precipitation method, shows superior activity with enhanced CO tolerance towards methanol production. The methanol STY reaches 0.569 $g_{methanol}$ g_{cat}^{-1} h^{-1} under the feed gas including 4% CO at 300 °C and 5 MPa with the GHSV of 21,000 $cm^3 \cdot h^{-1} \cdot g_{cat}^{-1}$, which is much higher than that of the Pt/In_2O_3

Table 3

Gibbs reaction energies (ΔG) and activation barrier (G_{ab}) of each elementary step in methanol production on the Pt_4/In_2O_3-ZrO_2 model (in eV).

No.	Reaction	G_{ab}	ΔG
R1	$CO_2 + * \rightarrow CO_2 *$	/	-0.44
R2	$H_2 + * + * \rightarrow 2 H*$	/	-2.77
R3	$CO_2 * \rightarrow CO* + O*$	0.25	-2.22
R4	$CO* + O* + H* \rightarrow CO* + OH* + *$	0.95	-0.63
R5	$CO* + OH* + H* -Zr \rightarrow CO* + OH* + H* -In$	1.22	+ 1.03
R6	$CO* + OH* + H* \rightarrow CO* + H_2O*$	0.42	+ 0.12
R7	$CO* + H_2O* \rightarrow CO* + H_2O(g) + *$	/	+ 1.03
R8	$CO* + H* \rightarrow HCO* + *$	0.46	-0.56
R9	$HCO* + H* \rightarrow H_2CO* + *$	0.74	-0.26
R10	$H_2CO* + H* \rightarrow H_3CO* + *$	0.20	-1.51
R11	$H_2CO* + H* \rightarrow H_2COH* + *$	0.62	+ 0.13
R12	$H_3CO* + H* \rightarrow H_3COH* + *$	1.15	+ 0.78
R13	$H_2COH* + H* \rightarrow H_3COH* + *$	2.29	-0.17
R14	$CO_2 * + H* \rightarrow COOH* + *$	0.46	+ 0.13
R15	$COOH* + H* \rightarrow CO* + H_2O(g) + *$	1.51	+ 0.38
R16	$CO* + H_2O(g) \rightarrow CO(g) + H_2O(g) + *$	/	+ 0.59
R17	$CO_2 * + H* \rightarrow HCOO* + *$	0.68	-0.92
R18	$HCOO* \rightarrow bi\text{-}HCOO*$	/	-0.40
R19	$HCOO* + H* \rightarrow H_2COO* + *$	1.05	+ 0.62
R20	$H_2COO* + H* \rightarrow H_2COOH* + *$	0.61	-0.02
R21	$H_2COOH* + H* \rightarrow H_2CO* + H_2O*$	0.83	+ 0.57
R22	$H_2CO* + H_2O* \rightarrow H_2CO* + H_2O(g) + *$	/	-0.21
R23	$H_2CO* + H_2O* + H* \rightarrow H_3CO* + H_2O* + *$	0.59	-1.25
R24	$H_2CO* + H_2O* + H* \rightarrow H_2COH* + H_2O* + *$	0.40	-0.14
R25	$H_3CO* + H_2O* + H* \rightarrow H_3COH* + H_2O* + *$	1.34	+0.89
R26	$H_2COH* + H_2O* + H* \rightarrow H_3COH* + H_2O* + *$	1.79	-0.23

catalyst (0.458 $g_{methanol}$ g_{cat}^{-1} h^{-1}). The results of XRD, XPS, Raman and EPR spectra confirm the In_2O_3-ZrO_2 support is in the form of solid solution. The catalyst characterizations also confirm the deactivation under the CO-containing feed gas is attributed to the over-reduction of In_2O_3 induced by CO. Based on the results of CO-TPD-MS and DFT calculations, CO adsorption is significantly weakened by the addition of ZrO_2, which results in the enhanced stability as well. The results of CO_2-TPD-MS profile also confirm the improved stability of surface oxygen atoms of In_2O_3 due to the presence of ZrO_2. Additionally, the electronic properties of oxygen vacancy are modified by ZrO_2 as well, which alters the active site for CO_2 activation from the interfacial site on the Pt/In_2O_3 catalyst to the In-O_v-Zr site on the Pt/In_2O_3-ZrO_2 catalyst. The synergy between the In-O_v-Zr site and Pt cluster leads to the alteration of methanol production from the CO hydrogenation route to the formate route. The present study shows that the Pt catalyst becomes highly active for CO_2 hydrogenation to methanol under the presence of CO with the In_2O_3-ZrO_2 solid solution as the support.

CRediT authorship contribution statement

Kaihang Sun: Investigation, Methodology, Data curation, Software, Writing – original draft. **Chenyang Shen:** Methodology, Software, Validation, Writing – review & editing. **Rui Zou:** Methodology, Validation. **Chang-jun Liu:** Conceptualization, Funding acquisition, Writing – review & editing, Supervision.

Declaration of Competing Interest

The authors declare that they have no known competing financial interests or personal relationships that could have appeared to influence the work reported in this paper.

Data availability

Data will be made available on request.

Appendix A. Supplementary material

Supplementary data associated with this article can be found in the online version at doi:10.1016/j.apcatb.2022.122018.

References

[1] X. Jiang, X. Nie, X. Guo, C. Song, J.G. Chen, Recent advances in carbon dioxide hydrogenation to methanol via heterogeneous catalysis, Chem. Rev. 120 (2020) 7984–8034, https://doi.org/10.1021/acs.chemrev.9b00723.

[2] B. Liang, J. Ma, X. Su, C. Yang, H. Duan, H. Zhou, S. Deng, L. Li, Y. Huang, Investigation on deactivation of Cu/ZnO/Al_2O_3 catalyst for CO_2 hydrogenation to methanol, Ind. Eng. Chem. Res. 58 (2019) 9030–9037, https://doi.org/10.1021/acs.iecr.9b01546.

[3] Y. Yan, R.J. Wong, Z. Ma, F. Donat, S. Xi, S. Saqline, Q. Fan, Y. Du, A. Borgna, Q. He, C.R. Müller, W. Chen, A.A. Lapkin, W. Liu, CO_2 hydrogenation to methanol on tungsten-doped Cu/CeO_2 catalysts, Appl. Catal. B 306 (2022), 121098, https://doi.org/10.1016/j.apcatb.2022.121098.

[4] J. Wang, J. Meeprasert, Z. Han, H. Wang, Z. Feng, C. Tang, F. Sha, S. Tang, G. Li, E. A. Pidko, C. Li, Highly dispersed Cd cluster supported on TiO_2 as an efficient catalyst for CO_2 hydrogenation to methanol, Chin. J. Catal. 43 (2022) 761–770, https://doi.org/10.1016/S1872-2067(21)63907-4.

[5] L.F. Rasteiro, R.A. De Sousa, L.H. Vieira, V.K. Ocampo-Restrepo, L.G. Verga, J. M. Assaf, J.L.F. Da Silva, E.M. Assaf, Insights into the alloy-support synergistic effects for the CO_2 hydrogenation towards methanol on oxide-supported Ni_5Ga_3 catalysts: an experimental and DFT study, Appl. Catal. B 302 (2022), 120842, https://doi.org/10.1016/j.apcatb.2021.120842.

[6] K. Lee, U. Anjum, T.P. Araújo, C. Mondelli, Q. He, S. Furukawa, J. Pérez-Ramírez, S.M. Kozlov, N. Yan, Atomic Pd-promoted ZnZrOx solid solution catalyst for CO_2 hydrogenation to methanol, Appl. Catal. B 304 (2022), 120994, https://doi.org/10.1016/j.apcatb.2021.120994.

[7] J. Ye, C. Liu, D. Mei, Q. Ge, Active oxygen vacancy site for methanol synthesis from CO_2 hydrogenation on In_2O_3(110): A DFT study, ACS Catal. 3 (2013) 1296–1306, https://doi.org/10.1021/cs400132a.

[8] K. Sun, Z. Fan, J. Ye, J. Yan, Q. Ge, Y. Li, W. He, W. Yang, C.-j Liu, Hydrogenation of CO_2 to methanol over In_2O_3 catalyst, J. CO_2 Util. 12 (2015) 1–6, https://doi.org/10.1016/j.jcou.2015.09.002.

[9] O. Martin, A.J. Martín, C. Mondelli, S. Mitchell, T.F. Segawa, R. Hauert, C. Drouilly, D. Curulla-Ferré, J. Pérez-Ramírez, Indium oxide as a superior catalyst for methanol synthesis by CO_2 hydrogenation, Angew. Chem. Int. Ed. 55 (2016) 6261–6265, https://doi.org/10.1002/anie.201600943.

[10] Q. Wu, C. Shen, N. Rui, K. Sun, C.-j Liu, Experimental and theoretical studies of CO_2 hydrogenation to methanol on Ru/In_2O_3, J. CO_2 Util. 53 (2021), 101720, https://doi.org/10.1016/j.jcou.2021.101720.

[11] J. Wang, K. Sun, X. Jia, C.-j Liu, CO_2 hydrogenation to methanol over Rh/In_2O_3 catalyst, Catal. Today 365 (2021) 341–347, https://doi.org/10.1016/j.cattod.2020.05.020.

[12] C. Shen, K. Sun, Z. Zhang, N. Rui, X. Jia, D. Mei, C.-j. Liu, Highly active Ir/In_2O_3 catalysts for selective hydrogenation of CO_2 to methanol: experimental and theoretical studies, ACS Catal. 11 (2021) 4036–4046, https://doi.org/10.1021/acscatal.0c05628.

[13] Z. Han, C. Tang, J. Wang, L. Li, C. Li, Atomically dispersed Pt^{n+} species as highly active sites in Pt/In_2O_3 catalysts for methanol synthesis from CO_2 hydrogenation, J. Catal. 394 (2021) 236–244, https://doi.org/10.1016/j.jcat.2020.06.018.

[14] M.S. Frei, C. Mondelli, R. García-Muelas, J. Morales-Vidal, M. Philipp, O. V. Safonova, N. López, J.A. Stewart, D.C. Ferré, J. Pérez-Ramírez, Nanostructure of nickel-promoted indium oxide catalysts drives selectivity in CO_2 hydrogenation, Nat. Commun. 12 (2021) 1960, https://doi.org/10.1038/s41467-021-22224-x.

[15] Z. Zhou, B. Qin, S. Li, Y. Sun, A DFT-based, microkinetic study on methanol synthesis from CO_2 hydrogenation over the In_2O_3 catalyst, Phys. Chem. Chem. Phys. 23 (2021) 1888–1895, https://doi.org/10.1039/D0CP05947A.

[16] N. Rui, F. Zhang, K. Sun, Z. Liu, W. Xu, E. Stavitski, S.D. Senanayake, J. A. Rodriguez, C.-J. Liu, Hydrogenation of CO_2 to methanol on a $Au^{\delta+}$-In_2O_{3-x} catalyst, ACS Catal. 10 (2020) 11307–11317, https://doi.org/10.1021/acscatal.0c02120.

[17] A. Pustovarenko, A. Dikhtiarenko, A. Bavykina, L. Gevers, A. Ramírez, A. Russkikh, S. Telalovic, A. Aguilar, J.-L. Hazemann, S. Ould-Chikh, J. Gascon, Metal-organic framework-derived synthesis of cobalt indium catalysts for the hydrogenation of CO_2 to methanol, ACS Catal. 10 (2020) 5064–5076, https://doi.org/10.1021/acscatal.0c00449.

[18] X. Jia, K. Sun, J. Wang, C. Shen, C.-j Liu, Selective hydrogenation of CO_2 to methanol over Ni/In_2O_3 catalyst, J. Energy Chem. 50 (2020) 409–415, https://doi.org/10.1016/j.jechem.2020.03.083.

[19] N.H.M.D. Dostagir, C. Thompson, H. Kobayashi, A.M. Karim, A. Fukuoka, A. Shrotri, Rh promoted In_2O_3 as a highly active catalyst for CO_2 hydrogenation to

methanol, Catal. Sci. Technol. 10 (2020) 8196–8202, https://doi.org/10.1039/D0CY01789B.

[20] S. Dang, B. Qin, Y. Yang, H. Wang, J. Cai, Y. Han, S. Li, P. Gao, Y. Sun, Rationally designed indium oxide catalysts for CO$_2$ hydrogenation to methanol with high activity and selectivity, Sci. Adv. 6 (2020) eaaz2060, https://doi.org/10.1126/sciadv.aaz2060.

[21] Z. Cai, J. Dai, W. Li, K.B. Tan, Z. Huang, G. Zhan, J. Huang, Q. Li, Pd supported on MIL-68(In)-derived In$_2$O$_3$ nanotubes as superior catalysts to boost CO$_2$ hydrogenation to methanol, ACS Catal. 10 (2020) 13275–13289, https://doi.org/10.1021/acscatal.0c03372.

[22] M.S. Frei, C. Mondelli, R. García-Muelas, K.S. Kley, B. Puértolas, N. López, O.V. Safonova, J.A. Stewart, D. Curulla Ferré, J. Pérez-Ramírez, Atomic-scale engineering of indium oxide promotion by palladium for methanol production via CO$_2$ hydrogenation, Nat. Commun. 10 (2019) 3377, https://doi.org/10.1038/s41467-019-11349-9.

[23] A. Tsoukalou, P.M. Abdala, D. Stoian, X. Huang, M.G. Willinger, A. Fedorov, C.R. Muller, Structural evolution and dynamics of an In$_2$O$_3$ catalyst for CO$_2$ hydrogenation to methanol: an operando XAS-XRD and in situ TEM study, J. Am. Chem. Soc. 141 (2019) 13497–13505, https://doi.org/10.1021/jacs.9b04873.

[24] M. Dou, M. Zhang, Y. Chen, Y. Yu, DFT study of In$_2$O$_3$-catalyzed methanol synthesis from CO$_2$ and CO hydrogenation on the defective site, New J. Chem. 42 (2018) 3293–3300, https://doi.org/10.1039/C7NJ04273F.

[25] K. Sun, N. Rui, C. Shen, C.-j Liu, Theoretical study of selective hydrogenation of CO$_2$ to methanol over Pt$_4$/In$_2$O$_3$ model catalyst, J. Phys. Chem. C 125 (2021) 10926–10936, https://doi.org/10.1021/acs.jpcc.1c00638.

[26] A. Cao, Z. Wang, H. Li, J.K. Nørskov, Relations between surface oxygen vacancies and activity of methanol formation from CO$_2$ hydrogenation over In$_2$O$_3$ surfaces, ACS Catal. 11 (2021) 1780–1786, https://doi.org/10.1021/acscatal.0c05046.

[27] N. Rui, Z. Wang, K. Sun, J. Ye, Q. Ge, C.-j Liu, CO$_2$ hydrogenation to methanol over Pd/In$_2$O$_3$: effects of Pd and oxygen vacancy, Appl. Catal. B 218 (2017) 488–497, https://doi.org/10.1016/j.apcatb.2017.06.069.

[28] K. Sun, N. Rui, Z. Zhang, Z. Sun, Q. Ge, C.-j. Liu, A highly active Pt/In$_2$O$_3$ catalyst for CO$_2$ hydrogenation to methanol with enhanced stability, Green. Chem. 22 (2020) 5059–5066, https://doi.org/10.1039/D0GC01597K.

[29] X. Ye, C. Yang, X. Pan, J. Ma, Y. Zhang, Y. Ren, X. Liu, L. Li, Y. Huang, Highly selective hydrogenation of CO$_2$ to ethanol via designed bifunctional Ir$_1$-In$_2$O$_3$ single-atom catalyst, J. Am. Chem. Soc. 142 (2020) 19001–19005, https://doi.org/10.1021/jacs.0c08607.

[30] K. Sun, Z. Zhang, C. Shen, N. Rui, C.-j Liu, The feasibility study of the indium oxide supported silver catalyst for selective hydrogenation of CO$_2$ to methanol, Green Energy Environ. 7 (2022) 807–817, https://doi.org/10.1016/j.gee.2021.05.004.

[31] J. Zhu, F. Cannizzaro, L. Liu, H. Zhang, N. Kosinov, I.A.W. Filot, J. Rabeah, A. Brückner, E.J.M. Hensen, Ni-In synergy in CO$_2$ hydrogenation to methanol, ACS Catal. 11 (2021) 11371–11384, https://doi.org/10.1021/acscatal.1c03170.

[32] J. Ye, C.-j Liu, D. Mei, Q. Ge, Methanol synthesis from CO$_2$ hydrogenation over a Pd$_4$/In$_2$O$_3$ model catalyst: a combined DFT and kinetic study, J. Catal. 317 (2014) 44–53, https://doi.org/10.1016/j.jcat.2014.06.002.

[33] C. Shen, Q. Bao, W. Xue, K. Sun, Z. Zhang, X. Jia, D. Mei, C.-j Liu, Synergistic effect of the metal-support interaction and interfacial oxygen vacancy for CO$_2$ hydrogenation to methanol over Ni/In$_2$O$_3$ catalyst: a theoretical study, J. Energy Chem. 65 (2022) 623–629, https://doi.org/10.1016/j.jechem.2021.06.039.

[34] X. Jiang, X. Nie, Y. Gong, C.M. Moran, J. Wang, J. Zhu, H. Chang, X. Guo, K.S. Walton, C. Song, A combined experimental and DFT study of H$_2$O effect on In$_2$O$_3$/ZrO$_2$ catalyst for CO$_2$ hydrogenation to methanol, J. Catal. 383 (2020) 283–296, https://doi.org/10.1016/j.jcat.2020.01.014.

[35] C. Yang, C. Pei, R. Luo, S. Liu, Y. Wang, Z. Wang, Z.-J. Zhao, J. Gong, Strong electronic oxide-support interaction over In$_2$O$_3$/ZrO$_2$ for highly selective CO$_2$ hydrogenation to methanol, J. Am. Chem. Soc. 142 (2020) 19523–19531, https://doi.org/10.1021/jacs.0c07195.

[36] A. Tsoukalou, P.M. Abdala, A. Armutlulu, E. Willinger, A. Fedorov, C.R. Müller, Operando X-ray absorption spectroscopy identifies a monoclinic ZrO$_2$:In solid solution as the active phase for the hydrogenation of CO$_2$ to methanol, ACS Catal. 10 (2020) 10060–10067, https://doi.org/10.1021/acscatal.0c01968.

[37] T.-y Chen, C. Cao, T.-b Chen, X. Ding, H. Huang, L. Shen, X. Cao, M. Zhu, J. Xu, J. Gao, Y.-F. Han, Unraveling highly tunable selectivity in CO$_2$ hydrogenation over bimetallic In-Zr oxide catalysts, ACS Catal. 9 (2019) 8785–8797, https://doi.org/10.1021/acscatal.9b01869.

[38] M.S. Frei, C. Mondelli, A. Cesarini, F. Krumeich, R. Hauert, J.A. Stewart, D. Curulla Ferré, J. Pérez-Ramírez, Role of zirconia in indium oxide-catalyzed CO$_2$ hydrogenation to methanol, ACS Catal. 10 (2020) 1133–1145, https://doi.org/10.1021/acscatal.9b03305.

[39] T. Numpilai, P. Kidkhunthod, C.K. Cheng, C. Wattanakit, M. Chareonpanich, J. Limtrakul, T. Witoon, CO$_2$ hydrogenation to methanol at high reaction temperatures over In$_2$O$_3$/ZrO$_2$ catalysts: influence of calcination temperatures of ZrO$_2$ support, Catal. Today 375 (2020) 298–306, https://doi.org/10.1016/j.cattod.2020.03.011.

[40] T.P. Araújo, A. Shah, C. Mondelli, J.A. Stewart, D. Curulla Ferré, J. Pérez-Ramírez, Impact of hybrid CO$_2$-CO feeds on methanol synthesis over In$_2$O$_3$-based catalysts, Appl. Catal. B 285 (2021) 119878, https://doi.org/10.1016/j.apcatb.2021.119878.

[41] J. Su, D. Wang, Y. Wang, H. Zhou, C. Liu, S. Liu, C. Wang, W. Yang, Z. Xie, M. He, Direct conversion of syngas into light olefins over zirconium-doped indium(III) oxide and SAPO-34 bifunctional catalysts: Design of oxide component and construction of reaction network, ChemCatChem 10 (2018) 1536–1541, https://doi.org/10.1002/cctc.201702054.

[42] G. Štefanić, S. Musić, S. Popović, A. Sekulić, FT-IR and laser Raman spectroscopic investigation of the formation and stability of low temperature t-ZrO$_2$, J. Mol. Struct. 408–409 (1997) 391–394, https://doi.org/10.1016/S0022-2860(96)09549-X.

[43] S. Tada, S. Kayamori, T. Honma, H. Kamei, A. Nariyuki, K. Kon, T. Toyao, K.-i Shimizu, S. Satokawa, Design of interfacial sites between Cu and amorphous ZrO$_2$ dedicated to CO$_2$-to-methanol hydrogenation, ACS Catal. 8 (2018) 7809–7819, https://doi.org/10.1021/acscatal.8b01396.

[44] Y.H. Wang, W.G. Gao, H. Wang, Y.E. Zheng, W. Na, K.Z. Li, Structure-activity relationships of Cu-ZrO$_2$ catalysts for CO$_2$ hydrogenation to methanol: interaction effects and reaction mechanism, RSC Adv. 7 (2017) 8709–8717, https://doi.org/10.1039/C6RA28305E.

[45] K. Samson, M. Śliwa, R.P. Socha, K. Góra-Marek, D. Mucha, D. Rutkowska-Zbik, J.F. Paul, M. Ruggiero-Mikołajczyk, R. Grabowski, J. Słoczyński, Influence of ZrO$_2$ structure and copper electronic state on activity of Cu/ZrO$_2$ catalysts in methanol synthesis from CO$_2$, ACS Catal. 4 (2014) 3730–3741, https://doi.org/10.1021/cs500979c.

[46] J. Gan, X. Lu, J. Wu, S. Xie, T. Zhai, M. Yu, Z. Zhang, Y. Mao, S.C.I. Wang, Y. Shen, Y. Tong, Oxygen vacancies promoting photoelectrochemical performance of In$_2$O$_3$ nanocubes, Sci. Rep. 3 (2013) 1021, https://doi.org/10.1038/srep01021.

[47] M. Mavrikakis, B. Hammer, J.K. Nørskov, Effect of strain on the reactivity of metal surfaces, Phys. Rev. Lett. 81 (1998) 2819–2822, https://doi.org/10.1103/PhysRevLett.81.2819.